Solid State Communications 278 (2018) 36–41

Contents lists available at ScienceDirect

Solid State Communications

journal homepage: www.elsevier.com/locate/ssc

Communication

Magnetic and magnetoelectric properties of hybrid-frustrated $Bi_2Ir_{2-x}Mn_xO_7$ pyrochlores

Dandan Liang [a,c], Hui Liu [b,*], Langsheng Ling [a], Lei Zhang [a], Changjin Zhang [a], Yuheng Zhang [a]

[a] High Magnetic Field Laboratory, Chinese Academy of Sciences, Hefei 230031, China
[b] Department of Mathematics and Physics, Hefei University, Hefei 230601, China
[c] University of Science and Technology of China, Hefei 230026, China

ARTICLE INFO

Communicated by H. Akai

Keywords:
A. Doped iridate
D. Electron localization
D. Magnetoresistance
D. 3d–5d electron interactions

ABSTRACT

The present paper investigates the magnetic and magnetoelectric properties of $Bi_2Ir_{2-x}Mn_xO_7$ compounds with respect to the degree of Mn doping denoted by x. It is found that the antiferromagnetic (AFM) interactions are initially enhanced with increasing x, but are then weakened with further increases in x. These findings are explained on the basis of the competition among AFM Ir–Ir, AFM Ir–Mn, and ferromagnetic Mn–Mn interactions. In addition, the electric transport properties at the temperature range studied present a metal-insulator transition in the range $0.05 \leq x \leq 0.15$, while an insulating state occurs for $x > 0.15$ because of electron localization. At low temperatures, a small positive magnetoresistance (MR) effect is observed for $x = 0$, whereas a negative MR effect is observed for all Mn-doped samples. The 3d–5d electron interactions play a dominant role in determining the magnetic properties of the doped samples.

1. Introduction

Recently, $A_2B_2O_7$ pyrochlore materials have been studied extensively because they exhibit a rich variety of unconventional ground states on the basis of magnetic frustration. In addition, the 5d transition metal oxides have attracted considerable attention because of their strong spin-orbit coupling (SOC). For Ir-based 5d oxides $A_2Ir_2O_7$ (A = Y, Bi, or a rare-earth element), the SOC, electronic correlation, and crystal field effect exhibit comparable energy scales. Therefore, these compounds are predicted to display a variety of unusual properties, such as the properties of a topological insulator, a Weyl semimetal, or a chiral spin liquid [1–5]. Numerous studies have also concentrated on $A_2B_2O_7$ systems based on 3d transition metals. These materials have attracted considerable attention owing to their interesting properties that include charge ordering, spin ordering, and orbital ordering. For example, $A_2Mn_2O_7$ pyrochlores exhibit ferromagnetic (FM) behavior with Curie temperatures between 20 and 40 K. The existence of ferromagnetism in this semiconductor indicates that metallic behavior is not a necessary condition for ferromagnetism in these compounds [6–8].

The coexistence of delocalized 5d and itinerant 3d magnetic sublattices in compounds provides an excellent framework to study the competition between SOC and/or super-exchange interactions and direct exchange. For example, Sr_3CuIrO_6 presents strong FM anisotropy arising from antiferromagnetic (AFM) super-exchange, which is rare in pure cuprates or iridates [9]. In the double perovskites Sr_2NiIrO_6 and Sr_2ZnIrO_6, the delocalized Ir 5d electrons produce long-range magnetic interactions, and the leading AFM interactions in the face-centered cubic (fcc) Ir sublattice give rise to a magnetic frustration in both materials [10]. However, few studies have focused on hybrid pyrochlore compounds of 3d–5d oxides, and issues related to the nature of the interactions between 3d and 5d ions and the effects on the ground state of the hybrid compounds have not been addressed.

To gain insights into the magnetic interactions of 3d–5d electrons in $A_2B_2O_7$ pyrochlores, the present study systematically investigates the hybrid pyrochlore $Bi_2Ir_{2-x}Mn_xO_7$ with nonmagnetic Bi^{3+} ions at the A-cation sites. Magnetization data show that the AFM interactions are initially enhanced with an increasing degree of Mn doping denoted by x, but eventually weaken with a further increase in x. This finding can be explained on the basis of the competition among AFM Ir–Ir, AFM Ir–Mn, and FM Mn–Mn interactions. The results also indicate that the electron transport properties tend toward those of an insulator because of electron localization. At low temperatures, a small positive magnetoresistance (MR) effect is observed in the parent material (i.e., for $x = 0$), whereas a negative MR effect is observed in all doped samples. The 3d–5d electron interactions play a dominant role in determining the magnetic properties of the doped samples.

* Corresponding author.
E-mail address: liuhui@hfuu.edu.cn (H. Liu).

https://doi.org/10.1016/j.ssc.2018.05.004
Received 28 April 2017; Received in revised form 11 April 2018; Accepted 14 May 2018
Available online 17 May 2018

2. Experiments

Polycrystalline samples of $Bi_2Ir_{2-x}Mn_xO_7$ ($x = 0$, 0.05, 0.1, 0.15, and 0.2) were synthesized by the solid-state reaction method. High-purity (>99.9%) stoichiometric amounts of Bi_2O_3, IrO_2, and MnO_2 powders were ground together and pelletized. The pellets were heated in air between 700 and 900 °C for 3 d with two intermediate grindings. After adding 5% IrO_2 in the appropriate molar ratio, the pellets were heated between 900 and 950 °C for 4 d with several intermediate grindings. The obtained samples were characterized by powder X-ray diffraction (XRD) with CuKα radiation at room temperature. The actual composition of the samples was determined by energy-dispersive x-ray (EDX) spectroscopy. Magnetic susceptibility measurements were conducted on a superconducting quantum interference device (SQUID) magnetometer (Quantum Design, Inc.). The electrical resistivity was measured by a conventional four-probe method. Electrical transport measurements were performed in DC magnetic fields of up to 9 T.

3. Results and discussion

The room-temperature XRD patterns shown in Fig. 1 indicate that the samples are single-phase with a cubic Fd-3m structure. The inset of Fig. 1 shows the evolution of the lattice parameter with respect to x. We note that the lattice parameter decreases with increasing x because the larger Ir^{4+} is increasingly substituted by the smaller Mn^{4+}. The EDX spectral analysis results show that all the samples are homogeneous with the actual compositions summarized in the second column of Table 1.

Fig. 2(a) presents the magnetic susceptibility χ versus temperature T curves for $Bi_2Ir_{2-x}Mn_xO_7$ samples in the temperature range of 2–300 K under a magnetic field $H = 1$ kOe. Only the zero field cooled (ZFC) modes are plotted in the figure because the ZFC and field-cooled (FC) modes were found to be overlapping. This demonstrates that all the samples followed the canonical paramagnetic behavior, with no magnetic ordering or spin-glass-like transition. The reciprocal magnetic ZFC susceptibility curves are shown in the inset of Fig. 2(a). At high temperatures (150–300 K), the inverse susceptibility data were fitted using the Curie-Weiss law

$$\chi = \frac{N_A \mu_{eff}^2}{3k_B(T - \theta_{CW})}, \quad (1)$$

where N_A is Avogadro's number, μ_{eff} is the effective magnetic moment, k_B is the Boltzmann constant, and θ_{CW} is the Curie-Weiss temperature. Columns 3 and 4 of Table 1 summarize the values of θ_{CW} and μ_{eff} obtained for the samples from the fitting to Eq. (1).

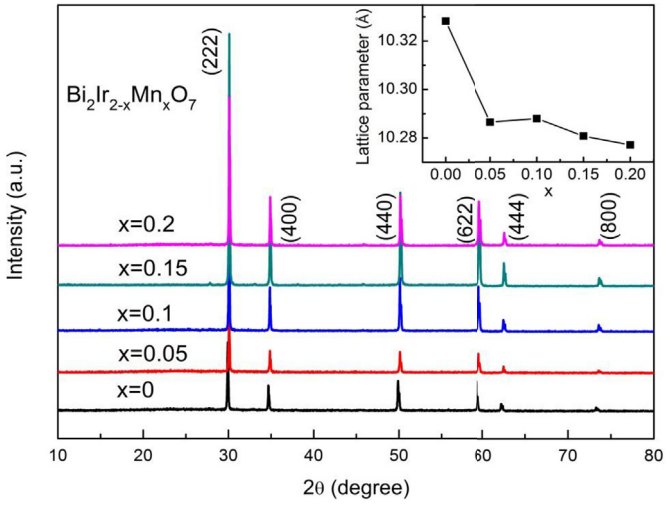

Fig. 1. XRD patterns of the $Bi_2Ir_{2-x}Mn_xO_7$ system. The inset shows the lattice parameters of the samples with respect to x.

The negative value of θ_{CW} obtained for $x = 0$ suggests an AFM correlation between Ir–Ir spins, which is consistent with previous reports [11,12]. The absolute value $|\theta_{CW}|$ increases at first and then decreases with increasing x. The initial increase in $|\theta_{CW}|$ can be attributed to AFM interactions between Ir and Mn ions. The decrease in $|\theta_{CW}|$ for $x > 0.1$ can be attributed to FM interactions in Mn–Mn networks. Thus, the non-monotonic variation in θ_{CW} indicates competition among the Ir–Ir, Ir–Mn, and Mn–Mn magnetic interactions. Because the Mn ions are very dilute in this substitution range, the interaction between Mn–Mn spins is weak. A small amount of Mn doping may not be sufficient to destroy the magnetic character (i.e., the AFM interactions between Ir atoms) of the parent material, which results in the presence of some short-range FM interactions in the system. Therefore, we consider that the 3d–5d electron interactions play an important role in determining the magnetic characteristics of the doped samples. Because the magnetic response is caused by the paramagnetic moments of Ir (μ_{Ir}) and Mn (μ_{Mn}), the theoretical value of μ_{eff} can be obtained by the expression

$$\mu_{eff}^2 = (2 - x)\mu_{Ir}^2 + x\mu_{Mn}^2. \quad (2)$$

Using the value $\mu_{Ir} = 0.24\mu_B$ of Ir^{4+} in $Bi_2Ir_2O_7$ and the value $\mu_{Mn} = 3.87\mu_B$ of free Mn^{4+}, we estimated the theoretical values of μ_{eff} (f.u.) for the $Bi_2Ir_{2-x}Mn_xO_7$ samples in column 5 of Table 1, and note that these values are close to the obtained experimental values in column 4 of Table 1. This finding demonstrates that the valence state of Mn in all doped samples is +4.

The magnetization M of the samples measured at $T = 2$ K with respect to H is presented in Fig. 2(b). Nearly complete saturation is observed for $x = 0$. However, the degree of unsaturation in the M–H curves becomes increasingly pronounced with increasing x. This finding indicates that the doped compounds have a tendency toward an enhanced AFM interaction, which is consistent with the results of the χ–T curves given in Fig. 2(a). The values of the saturation magnetization (M_{sat}; f.u.) of the samples are listed in the final column of Table 1. We note that the values of M_{sat} increase monotonically with increasing x. The estimated M_{sat} per Mn ion is $3.465\mu_B$, which is close to the theoretical value of $3\mu_B$ expected for Mn^{4+} ions with a $3d^3$ configuration, i.e., $S = 3/2$. The estimated value of M_{sat} per Mn ion being greater than the expected value may suggest strong coupling of the 3d–5d electrons.

Fig. 3 shows the zero field resistance ρ (relative to ρ at 300 K) versus T for the doped $Bi_2Ir_{2-x}Mn_xO_7$ samples. The behavior of ρ for the parent material $Bi_2Ir_2O_7$ (data not shown here) exhibited a weak metallic T-dependence that is similar to those of single crystal and thin film samples [11,13]. The metallic properties are caused by the accidental overlap between the Bi6s band and the Ir5d band [14,15]. Fig. 3 demonstrates that the ρ values of the doped samples are extremely sensitive to the Mn^{4+}/Ir^{4+} ratio because Mn-doping induces a metal-insulator transition in the range $0.05 \le x \le 0.15$, and a fully insulating state is obtained for the $x = 0.2$ sample. The metal-insulator transition temperature increases with increasing x, and, consequently, the transition temperature of the $x = 0.2$ sample is greater than 300 K.

As discussed, the substitution of Mn for Ir decreases the lattice parameter; thus, the Ir–O–Ir bond angle θ will also decrease with increasing x. A decreasing θ means that the elements of the hopping matrix should decrease and that the availability of conduction electrons reduces the screening of the Coulomb interaction. As a result, the bandgap will increase. Thus, the value of T at the metal-insulator transition T_{MI} increases monotonically [16]. The evolution of ρ with incrasing x can be explained by an increasing of grains boundaries caused by the introduction of Mn.

The electronic states involved in charge transport in a metal are spatially extended, whereas, in a nonmetal, these states are localized. The enhanced localization of electrons obtained with Mn-doping can also be obtained by increasing the effective value of μ_{Ir}. From Eq. (2), we note that, if the effective value of μ_{Mn} is maintained at $3.87\mu_B$, the calculated

Table 1
Nominal composition, actual composition, Curie-Weiss temperature θ_{CW}, effective moment μ_{eff}, and saturated magnetic moment M_{sat} of the $Bi_2Ir_{2-x}Mn_xO_7$ system.

Nominal composition	Actual composition	θ_{CW} (K)	μ_{eff} ($\times\mu_B$; f.u.) Experimental	μ_{eff} ($\times\mu_B$; f.u.) Theoretical	M_{sat} ($\times\mu_B$; f.u.)
$Bi_2Ir_2O_7$	$Bi_{2.028}Ir_{1.972}$	−2.05	0.34	–	0.013
$Bi_2Ir_{1.95}Mn_{0.05}O_7$	$Bi_{1.932}Ir_{2.012}Mn_{0.055}$	−20.61	1.42	1.90	0.208
$Bi_2Ir_{1.9}Mn_{0.1}O_7$	$Bi_{1.916}Ir_{1.981}Mn_{0.102}$	−13.57	1.88	2.05	0.369
$Bi_2Ir_{1.85}Mn_{0.15}O_7$	$Bi_{1.873}Ir_{2.002}Mn_{0.125}$	1.45	2.16	2.19	0.523
$Bi_2Ir_{1.8}Mn_{0.2}O_7$	$Bi_{1.898}Ir_{1.936}Mn_{0.165}$	−2.17	2.45	2.32	0.611

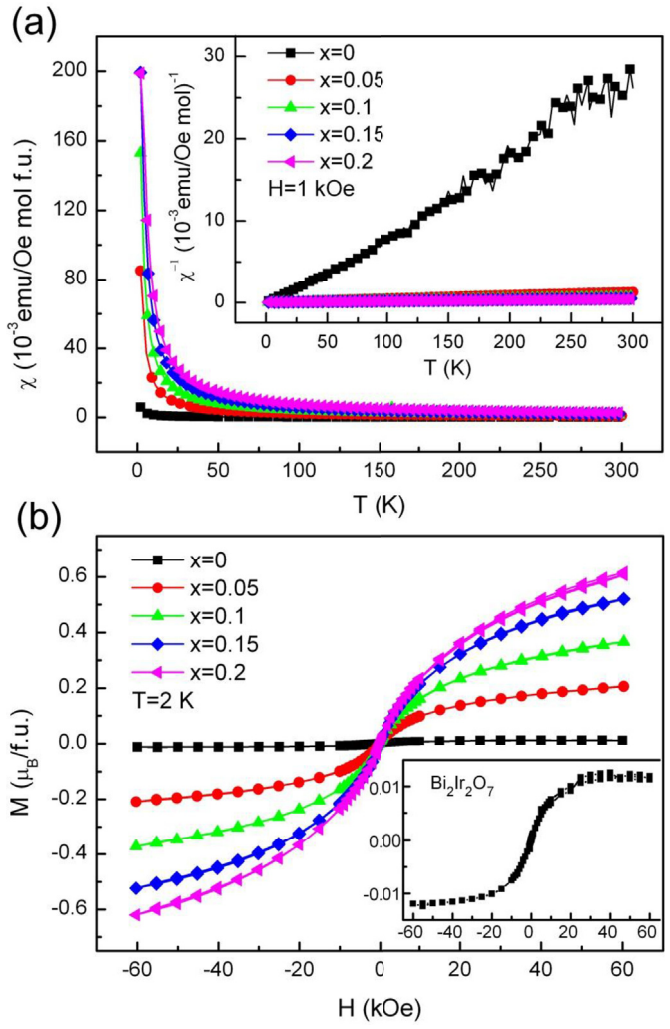

Fig. 2. (a) Zero field cooled (ZFC) susceptibility χ versus temperature T of the $Bi_2Ir_{2-x}Mn_xO_7$ system for a magnetic field $H = 1$ kOe. The inset shows the corresponding inverse DC susceptibility χ^{-1}. (b) Isothermal magnetization M-H curves at $T = 2$ K. The inset shows the low-field curves for the parent sample (i.e., $x = 0$).

values of μ_{Ir} are $0.80\mu_B$, $1.04\mu_B$, $1.16\mu_B$, and $1.29\mu_B$ for the $x = 0.05$, 0.1, 0.15, and 0.2 samples, respectively, which means that the localization of electrons is enhanced with Mn-doping, and the insulating behavior becomes increasingly more significant. The localization of the electrons in a crystalline material can be caused by the following conditions: static disorder; a strong local electron–electron correlation that "freezes" the local electron number; or a strong electron-lattice coupling, which traps the electrons locally [17].

To better understand the nature of the conduction mechanism for the Mn-doped samples in the metallic region, we fit the $\rho(T)$ data using the following empirical equation [18,19].

$$\rho = \rho_0 + \rho_2 T^2 + \rho_{4.5} T^{4.5} \quad (3)$$

Here, ρ_0 represents the resistivity caused by grain boundary effects, the second term $\rho_2 T^2$ indicates resistivity caused by the electron–electron scattering process, and the last term $\rho_{4.5} T^{4.5}$ is a combination of the electron–electron, electron–phonon, and electron–magnon scattering processes. The fitting results in the metallic region are also presented in Fig. 3. We find that the conductivity data for the $x = 0.05$, 0.1, and 0.15 samples in the metallic regime fit the equation well. However, in this short-ranged magnetic order case, there cannot be magnons, so the spin fluctuation (i.e. AFM and/or FM short-range correlations) scattering instead of magnon scattering exists in the system. Thus we suggest that the transport mechanism of this regime is attributed to grain boundary effects, electron– (electron, phonon and spin fluctuation) scattering processes.

We also fitted the $\rho(T)$ data of the Mn-doped samples in the insulating regime. For the samples with $x = 0.05$, ρ follows a thermally activated exponential behavior $\rho = \rho_0 \exp(E/k_BT)$, which is plotted in Fig. 4(a), whereas ρ for the $x \geq 0.1$ samples can be fitted by Mott's variable-range hopping (VRH) model $\rho = \rho_0 \exp(T_0/T)^{1/4}$, which are plotted in Fig. 4(b), (c), and (d). The results suggest that the transport mechanism transits from thermal activation to variable-range hopping with an increasing concentration of Mn ions. With increasing x, the itinerant e_g electrons of the Ir^{4+} ions are more localized, and the activation energy becomes very large. Thus, the e_g electrons cannot hop, which prevents the thermal activation route from dominating the transport behavior for $x \geq 0.1$. Simultaneously, the electron spins form a random magnetic structure caused by Ir-Mn interactions. Hence, ρ in the insulating regime can be fitted by Mott's VRH model [20].

Important information regarding electronic scattering processes can be obtained from MR data. The MR is denoted as $\Delta R/R_0 = (R_H - R_0)/R_0$, where R_H and R_0 are the resistivity values obtained at a given value of H and at $H = 0$, respectively. The values measured at $T = 2$ K with respect to H from −8 T to 8 T are shown in Figs. 5 and 6 for $x = 0$ and Mn-doped samples, respectively. We noticed that some MR curves are not exactly symmetrical, which may be caused by an imperfect measurement. In the measurement process, we collected the data of transverse magnetoresistance using standard four-probe method (see Fig. 7). Two of the probes are used to measure voltage (2 and 3) and the other two probes are used to source current (1 and 4). If the probes of voltage and the probes of current are not in a straight line, the additional Hall component will appear. Thus we consider that the asymmetric behavior of $\Delta R/R_0$-H curves may be due to the misalignment of four probes.

For the parent material $Bi_2Ir_2O_7$ in Fig. 5, the MR is positive, and increases with increasing H without any tendency toward saturation. For $H < 4$ T, the MR increases abruptly with increasing H, and follows a quadratic H-dependence, which is related to the low-field MR effect. At $H \geq 4$ T, the MR increases almost linearly with respect to H, but with a reduced slope. The obvious transition occurs in the MR from the quadratic H-dependence at low H to the linear H-dependence at high H, as is expected theoretically for Weyl semimetals [21]. We also find that the H-dependence of the MR in the polycrystalline $Bi_2Ir_2O_7$ sample is not consistent with those of previously reported single crystal and thin film samples [13], where a linearly dependent MR was obtained at low T. This difference could be caused by sample dependence. Compared with the single-crystal samples, the polycrystalline samples are less homogeneous

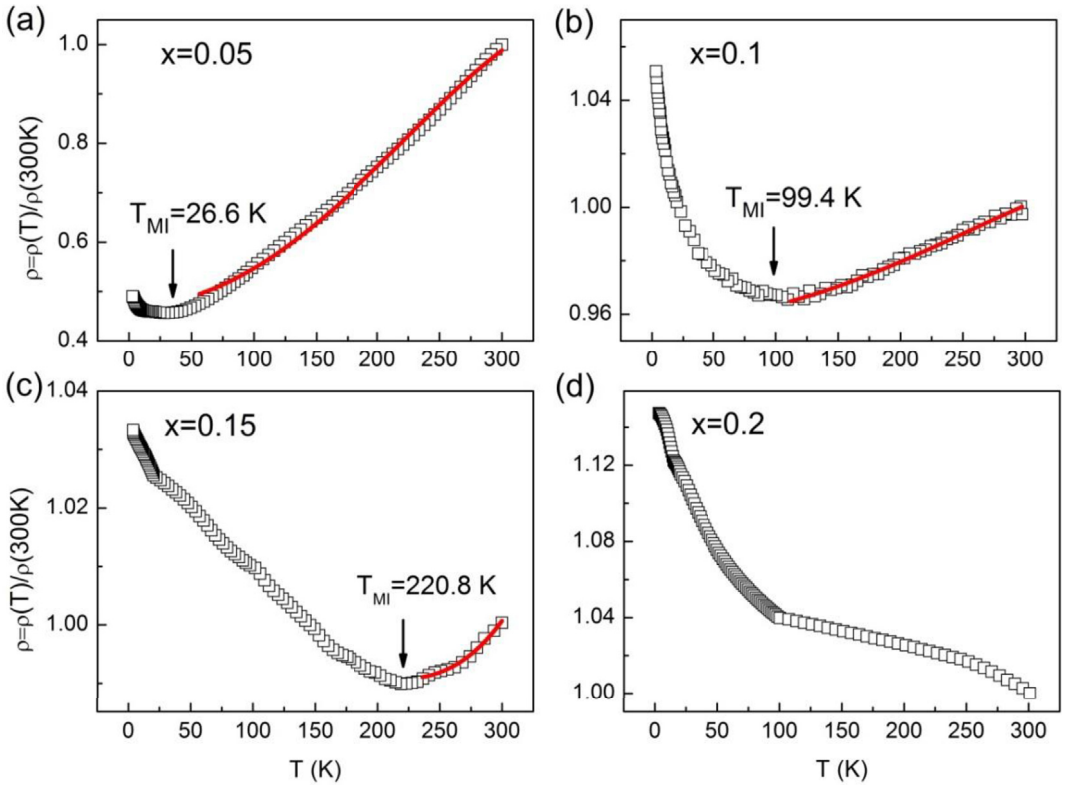

Fig. 3. Zero field resistance ρ (relative to ρ at 300 K) versus T for the doped $Bi_2Ir_{2-x}Mn_xO_7$ samples. The red lines are the results of fitting to Eq. (3). (For interpretation of the references to colour in this figure legend, the reader is referred to the Web version of this article.)

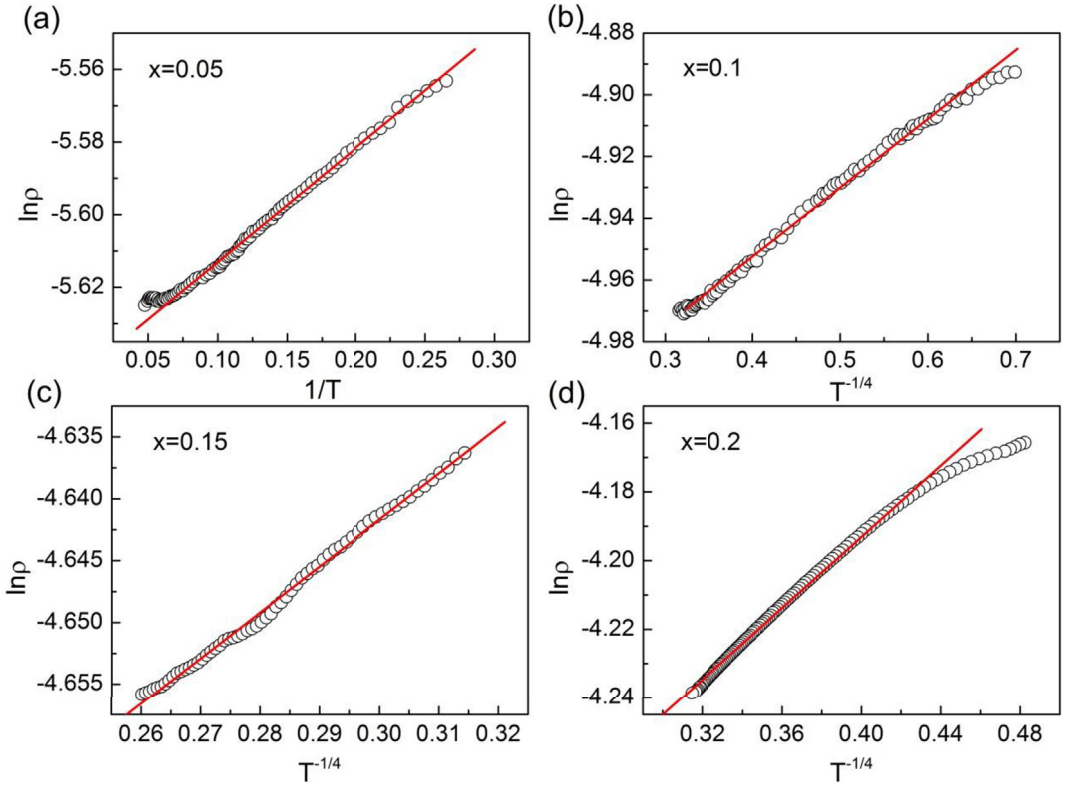

Fig. 4. Fitting of the values of lnρ for doped $Bi_2Ir_{2-x}Mn_xO_7$ samples: (a) lnρ versus 1/T curve for the $x = 0.05$ sample based on a thermally activated exponential behavior; (b)–(d) lnρ versus $T^{-1/4}$ curves for the $Bi_2Ir_{2-x}Mn_xO_7$ samples with $x = 0.1$, 0.15, and 0.2, respectively, based on Mott's variable-range hopping model.

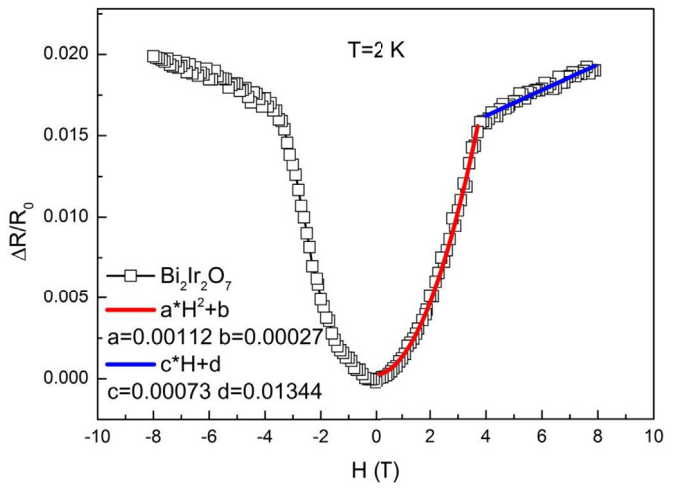

Fig. 5. Isothermal magnetoresistance $\Delta R/R_0$ versus H for the $Bi_2Ir_2O_7$ sample measured at $T = 2$ K. The red and blue lines are quadratic and linear fits of the $\Delta R/R_0$ dependence on H, respectively. (For interpretation of the references to colour in this figure legend, the reader is referred to the Web version of this article.)

because the oxygen vacancies or defects are formed during heating process. The roles of oxygen content and chemical disorder are very crucial on the electrical as well as the magnetic properties. In this case, the difference between the polycrystalline material and single crystal material results from chemical disorder and oxygen deficiency.

A small positive MR effect was observed for the $Bi_2Ir_2O_7$ sample, while a negative MR effect was obtained for the doped samples at $T = 2$ K, as shown in Fig. 6. To understand the reason for this observed behavior, the H-dependence of the observed MR for the doped samples was fitted with the empirical relation [17,22]:

$$\Delta R/R_0 = -\alpha H^n, \tag{4}$$

where α is the strength of MR and n is an empirical exponent. The values of α and n were obtained from fitting to the data in Fig. 6, and are listed in Table 2.

We find from Table 2 that the value of α increases with increasing x. In a completely paramagnetic state, $n = 2$, and the deviation from $n = 2$ indicates the existence of short-range correlations [17]. The obtained values of $n < 1$ demonstrate that the magnetic frustration arises in the doped samples because of directly competing FM and AFM exchange interactions [22], *i.e.*, competition among AFM Ir–Ir, AFM Ir–Mn, and FM

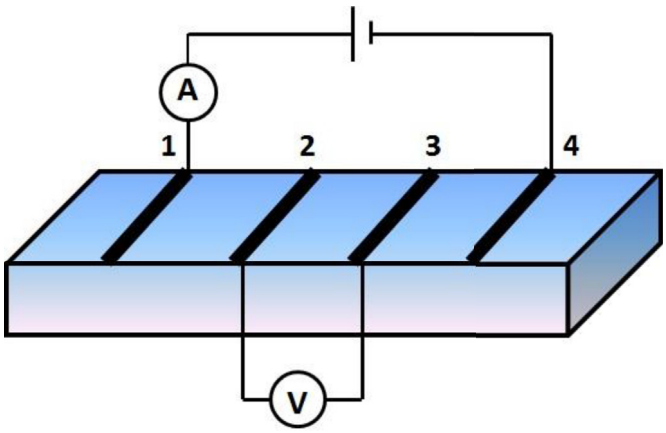

Fig. 7. Schematic diagram of the standard four-probe method.

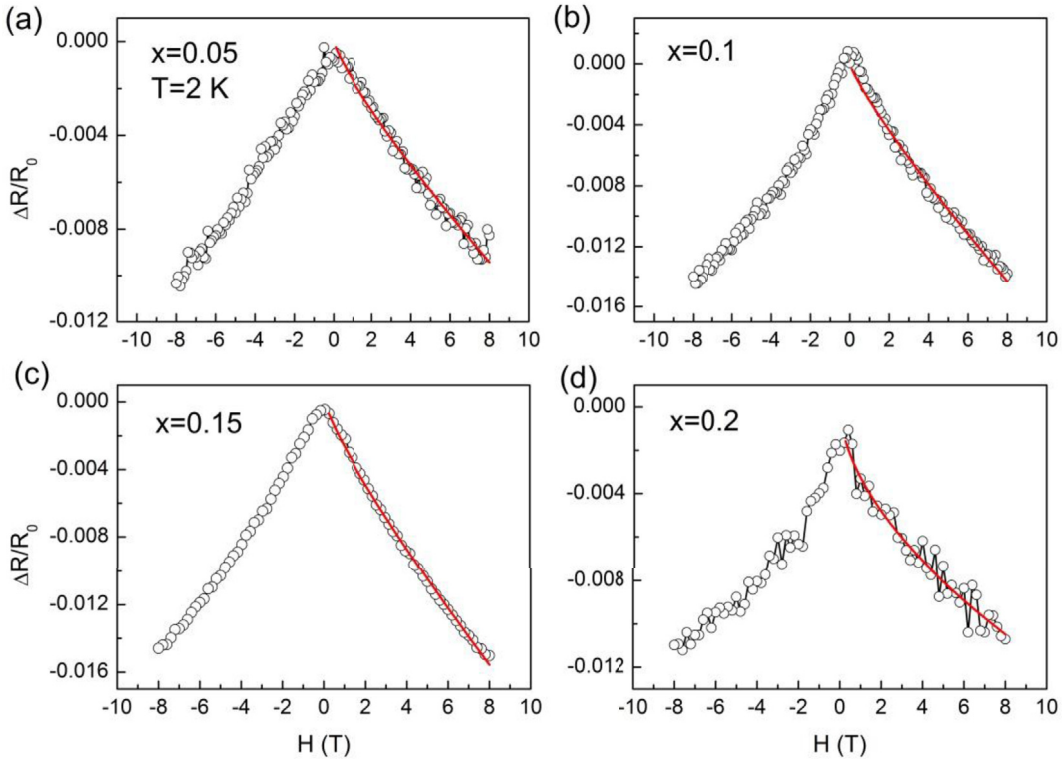

Fig. 6. Isothermal values of $\Delta R/R_0$ versus H at $T = 2$ K. The solid red lines show the results of fitting to the experimental data using Eq. (4). (For interpretation of the references to colour in this figure legend, the reader is referred to the Web version of this article.)

Table 2
Values of parameters n and α obtained from fitting the data in Fig. 6 to Eq. (4).

x	n	α (T^{-n})
0.05	0.84	1.65×10^{-3}
0.1	0.85	2.42×10^{-3}
0.15	0.84	2.69×10^{-3}
0.2	0.56	3.27×10^{-3}

Mn–Mn interactions. It is of interest that the values of n are very nearly equivalent (i.e., 0.84 ± 0.01) for the $x = 0.05$, 0.1, and 0.15 samples, whereas, on further doping to 0.2, n decreases to 0.56. Therefore, the MR values of samples with $x \leq 0.15$ exhibit contributions from both intercluster interactions, which are of a spin-glass type, and intracluster interactions, which are FM. However, the decreased value of n for the $x = 0.2$ sample can be attributed to fluctuations caused by the formation of clusters [22]. The functional relation between MR and H given by Eq. (4) with distinct values of α and n have been found for different magnetic phases.

When the Ir^{4+} ions are substituted by the Mn^{4+} ions, the 3d–5d interactions lead to a finite internal field at the Mn sites. The internal field will fluctuate the all-in/all-out state of Ir moments, resulting in the disorder in the magnetic structure of the system. As the applied magnetic field increases, the spins of Ir and Mn electrons with different directions become parallel. Correspondingly, the disorder in the magnetic structure is suppressed and the contribution of carriers scattering is decreased. Consequently, the electrical resistivity of the compounds is also decreased. Thus, a negative MR effect is obtained.

4. Conclusion

In summary, we have investigated the magnetic and magnetoelectric properties of $Bi_2Ir_{2-x}Mn_xO_7$ compounds. The non-monotonic evolution of magnetic interactions with respect to doping content was demonstrated to be caused by competition among AFM Ir–Ir, AFM Ir–Mn, and FM Mn–Mn interactions. The zero field resistivity presented a metal–insulator transition for samples in the range $0.05 \leq x \leq 0.15$, and a fully insulating state was obtained for the $x = 0.2$ sample. At low temperatures, a small positive MR effect was observed in the parent material (i.e., $x = 0$), whereas a negative MR effect was observed in the Mn-doped samples. The results demonstrated that 3d–5d electron interactions play a dominant role in determining the magnetic properties of the doped samples.

Acknowledgments

This work was supported by the National Key Research and Development Program of China (Grant No. 2016YFA0300404), the National Natural Science Foundation of China (Grant Nos. U1532267, 11674327, and 11604071), and the Natural Science Foundation of Hefei University (Grant Nos. 16ZR06ZDB and 2017jyxm013).

References

[1] B.-J. Yang, Y.B. Kim, Phys. Rev. B 82 (2010), 085111.
[2] X. Wan, A.M. Turner, A. Vishwanath, S.Y. Savrasov, Phys. Rev. B 83 (2011), 205101.
[3] J.C. Gallagher, B.D. Esser, R. Morrow, S.R. Dunsiger, R.E.A. Williams, P.M. Woodward, D.W. McComb, F.Y. Yang, Sci. Rep. 6 (2016) 22282, https://doi.org/10.1038/srep22282.
[4] A.B. Sushkov, J.B. Hofmann, G.S. Jenkins, J. Ishikawa, S. Nakatsuji, S. Das Sarma, H.D. Drew, Phys. Rev. B 92 (2015) 241108(R).
[5] L. Balicas, S. Nakatsuji, Y. Machida, S. Onoda, Phys. Rev. Lett. 106 (2011), 217204.
[6] J.E. Greedan, N.P. Raju, A. Maignan, Ch Simon, J.S. Pedersen, A.M. Niraimathi, E. Gmelin, M.A. Subramanian, Phys. Rev. B 54 (1996) 7189.
[7] N. Imamura, M. Karppinen, H. Yamauchi, J.B. Goodenough, Phys. Rev. B 82 (2010), 132407.
[8] N. Imamura, M. Karppinen, H. Yamauchi, Solid State Commun. 144 (2007) 98.
[9] Wei-Guo Yin, X. Liu, A.M. Tsvelik, M.P.M. Dean, M.H. Upton, Jungho Kim, D. Casa, A. Said, T. Gog, T.F. Qi, G. Cao, J.P. Hill, Phys. Rev. Lett. 111 (2013), 057202.
[10] Xuedong Ou, Zhengwei Li, Fengren Fan, Hongbo Wang, Hua Wu, Sci. Rep. 4 (2014) 7542, https://doi.org/10.1038/srep07542.
[11] T.F. Qi, O.B. Korneta, Xian Gang Wan, L.E. DeLong, P. Schlottmann, G. Cao, J. Phys. Condens. Matter 24 (2012), 345601.
[12] P.J. Baker, J.S. Möller, F.L. Pratt, W. Hayes, S.J. Blundell, T. Lancaster, T.F. Qi, G. Cao, Weak magnetic transitions in pyrochlore $Bi_2Ir_2O_7$, Phys. Rev. B 87 (2013) 180409(R).
[13] Jiun-Haw Chu, Scott C. Riggs, Maxwell Shapiro, Jian Liu, Claudy Ryan Serero, Di Yi, M. Melissa, S. J. Suresha, C. Frontera, Ashvin Vishwanath, Xavi Marti, I. R. Fisher, R. Rameshar, (2013) arXiv:1309.4750.
[14] Y.S. Lee, S.J. Moon, Scott C. Riggs, M.C. Shapiro, I.R. Fisher, Bradford W. Fulfer, Julia Y. Chan, A.F. Kemper, D.N. Basov, Phys. Rev. B 87 (2013), 195143.
[15] Daniel P. Shoemaker, Ram Seshadri, Andrew L. Hector, Makoto Tachibana, Phys. Rev. B 84 (2011), 064117.
[16] L. Li, P.P. Kong, T.F. Qi, C.Q. Jin, S.J. Yuan, L.E. DeLong, P. Schlottmann, G. Cao, Phys. Rev. B 87 (2013), 235127.
[17] P. Dutta, S. Pramanick, Vijay Singh, Dan Thomas Major, D. Das, S. Chatterjee, Phys. Rev. B 93 (2016), 134408.
[18] E. Zghal, M. Koubaa, P. Berthet, L. Sicard, W. Cheikhrouhou-Koubaa, C. Decorse-Pascanut, A. Cheikhrouhou, S. Ammar-Merah, J. Magn. Magn Mater. 414 (2016) 97.
[19] Neeraj Panwar, Vikram Sen, D.K. Pandya, S.K. Agarwal, Mater. Lett. 61 (2007) 4879.
[20] L. Pi, L. Zheng, Y. Zhang, Phys. Rev. B 61 (2001) 8917.
[21] N. Ramakrishnan, M. Milletari, S. Adam, Phys. Rev. B 92 (2015), 245120.
[22] T.K. Nath, A.K. Majumdar, Phys. Rev. B 57 (1998) 10655.